Available online at www.sciencedirect.com
ScienceDirect
Trans. Nonferrous Met. Soc. China 30(2020) 928−943
Transactions of Nonferrous Metals Society of China
www.tnmsc.cn

Relationship among microstructure, mechanical properties and texture of TA32 titanium alloy sheets during hot tensile deformation

Rong-lei FAN, Yong WU, Ming-he CHEN, Lan-sheng XIE

National Key Laboratory of Science and Technology on Helicopter Transmission, Nanjing University of Aeronautics and Astronautics, Nanjing 210016, China

Received 6 July 2019; accepted 16 March 2020

Abstract: The relationship among microstructure, mechanical properties and texture of TA32 titanium alloy sheets during hot tensile deformation at 800 °C was investigated. In the test, the original sheet exhibited relatively low flow stress and sound plasticity, and increasing the heat treatment temperature resulted in an increased ultimate tensile strength (UTS) and a decreased elongation (EL). The deformation mechanism of TA32 alloy was dominated by high angle grain boundaries sliding and coordinated by dislocation motion. The coarsening of grains and the annihilation of dislocations in heat-treated specimens weakened the deformation ability of material, which led to the increase in flow stress. Based on the high-temperature creep equation, the quantitative relationship between microstructure and flow stress was established. The grain size exponent and α phase strength constant of TA32 alloy were calculated to be 1.57 and 549.58 MPa, respectively. The flow stress was accurately predicted by combining with the corresponding phase volume fraction and grain size. Besides, the deformation behavior of TA32 alloy was also dependent on the orientation of predominant α phase, and the main slip mode was the activation of prismatic $\langle a \rangle$ slip system. The decrease of near prism-oriented texture in heat-treated specimens resulted in the enhancement of strength of the material.

Key words: TA32 titanium alloy sheets; hot tensile deformation; microstructure evolution; mechanical properties; texture

1 Introduction

Titanium alloys are extensively used in the aerospace, marine and automotive industries because of their excellent properties [1,2]. Among various titanium alloys, the near-α titanium alloys are often used as blades and compressor discs due to the advances of superior fatigue and creep properties [3]. However, owing to their poor ductility at room temperature, most of titanium alloys are processed by hot forming process [4,5]. It is well known that the deformation behaviors of materials are intrinsically related to their microstructures, and changes of microstructure during hot forming process can significantly influence mechanical properties and deformation mechanisms [6]. Besides, because of the hexagonal close packed (HCP) structure of α phase, intense texture often exists in titanium alloys, especially in near-α titanium alloys, which also plays an essential role in the deformation behavior of material [7−9]. Therefore, it is necessary to study the evolution of microstructure and texture during hot tensile deformation and their effect on tensile properties.

In recent years, researches on deformation behavior of near-α high-temperature titanium alloy have gradually increased [10,11], and the microstructure changes and deformation mechanisms of a number of high-temperature titanium alloys during deformation have been studied [12−14], which promotes the development of forming theory and process of such high-temperature alloy. However, during hot forming process, titanium alloy sheet

Foundation item: Project (51805256) supported by the National Natural Science Foundation of China
Corresponding author: Yong WU; Tel: +86-17826026738; E-mail: wuyong@nuaa.edu.cn
DOI: 10.1016/S1003-6326(20)65266-9

usually needs to be held at the forming temperature in the furnace for a long time before deformation, which is equivalent to a heat treatment of the sheet. And local temperature non-uniformity in furnace and molds will lead to the inhomogenous microstructures of the sheet, which will further affect the subsequent deformation behavior. In order to accurately predict the plastic forming of a complex part and optimize the process parameters, it is essential to quantitatively describe the relationship between various microstructure features and corresponding material strength. Fortunately, unified viscoplastic constitutive equations [15−17], based on internal physical variables, can offer a good idea to quantitatively describe the relationship among the strain rate, grain size, phase volume fractions, damage, dislocation, flow stress and so on. In addition, it is widely accepted that the mechanical properties of titanium alloys also depend on the orientation of the grains [3,18,19], which has been rarely investigated in a near-α TA32 titanium alloy sheet during hot deformation.

In this study, the TA32 titanium alloy sheets were heat-treated with varying temperatures to obtain various microstructure features, and the original and heat-treated sheets were tested at a deformation temperature of 800 °C and an initial strain rate of 0.001 s^{-1}. The volume fractions and grain sizes of α and β phases of the tested specimens were quantitatively analyzed. The effects of phase volume fractions and grain sizes on the flow stress were described by the creep equation. Electron back-scattered diffraction (EBSD) technique was used to observe the microstructure and texture evolution during hot tensile deformation. The deformation mechanism and slip mode of TA32 alloy were discussed deeply to interpret different evolutions of tensile properties of specimens with increasing heat treatment temperature. The aim of this study was to provide basic data for the physically-based constitutive equation and to understand the relationship among microstructure, mechanical properties and texture in TA32 titanium alloy sheets during hot tensile deformation.

2 Experimental

The TA32 sheet with the nominal composition of Ti−5.5Al−3.5Sn−3.0Zr−0.7Mo−0.3Si−0.4Nb−0.4Ta (in at.%) and a thickness of 1.5 mm was utilized in this work [20,21]. The β-transus temperature was (1000±10) °C [10,21]. The microstructure observation of the sheet during hot tensile deformation was characterized by optical microscope (OM) and EBSD technique. Since the content of β phase in TA32 titanium alloy cannot be calibrated accurately by EBSD software, the volume fraction and average grain size of β phase in this work were calculated by measuring optical microstructure using image Pro Plus 6.0 software. The specimens for EBSD measurement were electro-polished with a solution of 60% methanol, 34% butanol and 6% perchloric acid (in volume fraction) at −40 °C and 30 V. Kroll reagent (5% HF, 10% HNO_3 and 85% H_2O, in volume fraction) was used for the metallographic observation. The EBSD data were obtained using a ZEISS Supra 55 SAPPHIRE scanning electron microscope with 0.2 μm step size, and analyzed through the HKL-Channel 5 software.

Tensile specimens with a gauge length of 25 mm and a width of 6 mm were machined from the sheet along the rolling direction (RD), as shown in Fig. 1(a). In order to obtain various heat-treated TA32 sheets, as shown in Table 1, the specimens were divided into four groups: the original specimen and three heat-treated specimens with different heat treatment temperatures. Each group of specimens was sealed in a vacuum glass tube for heat treatment, and followed by quenching in water to preserve the microstructure.

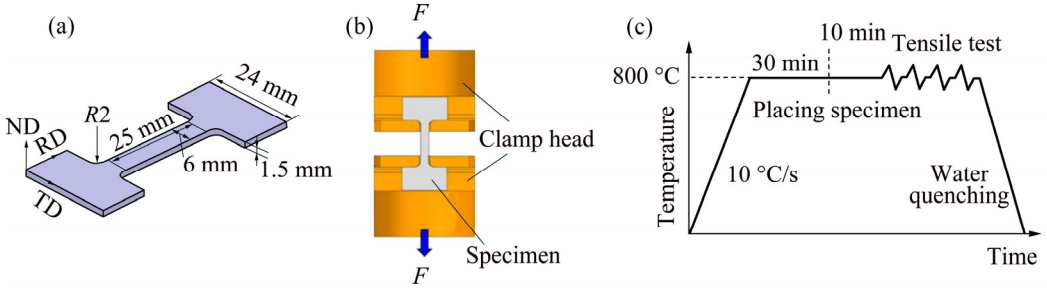

Fig. 1 Tensile specimen (a), hot tensile fixtures (b) and schematic diagram of tensile test (c)

Table 1 Several different heat treatment conditions and tensile schemes

Test No.	Heat treatment condition	Tensile test parameter	Tensile strain
Test-0	Original	800 °C, 0.001 s^{-1}	0.45 and fracture
Test-1	800 °C, 2 h	800 °C, 0.001 s^{-1}	0.45 and fracture
Test-2	850 °C, 2 h	800 °C, 0.001 s^{-1}	0.45 and fracture
Test-3	900 °C, 2 h	800 °C, 0.001 s^{-1}	0.45 and fracture

All the specimens were carried out on a UTM 5504X electronic universal testing machine at 800 ºC with a strain rate of 0.001 s^{-1}. Fixtures and schematic diagram of hot tensile test are shown in Figs. 1(b) and (c), respectively. The furnace was heated to the test temperature at a heating rate of 10 ºC/s, and the temperature was maintained for 30 min so that the temperature of the clamp head and the furnace chamber could be sufficiently exchanged. Then, we opened the furnace door and quickly placed the specimen, the soaking time before the tension was about 10 min to eliminate the temperature gradient. Tensile specimens of each heat treatment condition were stretched to a true strain of 0.45 and fractured, respectively. After the process, specimens were immediately quenched in water to retain the deformation microstructure. All the results were tested three times to reduce the error.

3 Results and discussion

3.1 Initial materials and tensile properties

The optical microstructure and the inverse pole figure (IPF) of the initial materials are shown in Figs. 2(a) and (b), respectively, in which the color code represents orientations of α grains, black lines represent high angle grain boundaries (HAGBs, θ>15°), blue lines represent low angle grain boundaries (LAGBs, 2°<θ<15°), and the region in black represents the β phase. The initial sheet consists of predominant equiaxed α phase and intergranular β phase, and the fraction of β phase is <5%. Figure 2(c) shows the grain size distribution of the initial materials, which indicates that the initial sheet has a large inhomogeneity of grain size, and the average size of α phase is 2.23 μm. Figure 2(d) shows the misorientation distribution of the initial sheet, where the fraction of LAGBs reaches up to 58.9%. The abundant internal LAGBs indicate that the initial sheet contains substantial prior deformation substructures. Besides, according to the pole figures (PFs) of initial sheet as shown in Fig. 2(e), two main texture components appear in the sheet: A $(\bar{1}2\bar{1}2)[10\bar{1}0]$ and B $(\bar{1}2\bar{1}5)[1\bar{2}13]$, where texture A is a typical texture of rolled titanium sheets with the maximum texture intensity of 23.72 [22].

Figure 3(a) shows the true stress−strain curves of uniaxial tensile test at 800 °C with a strain rate

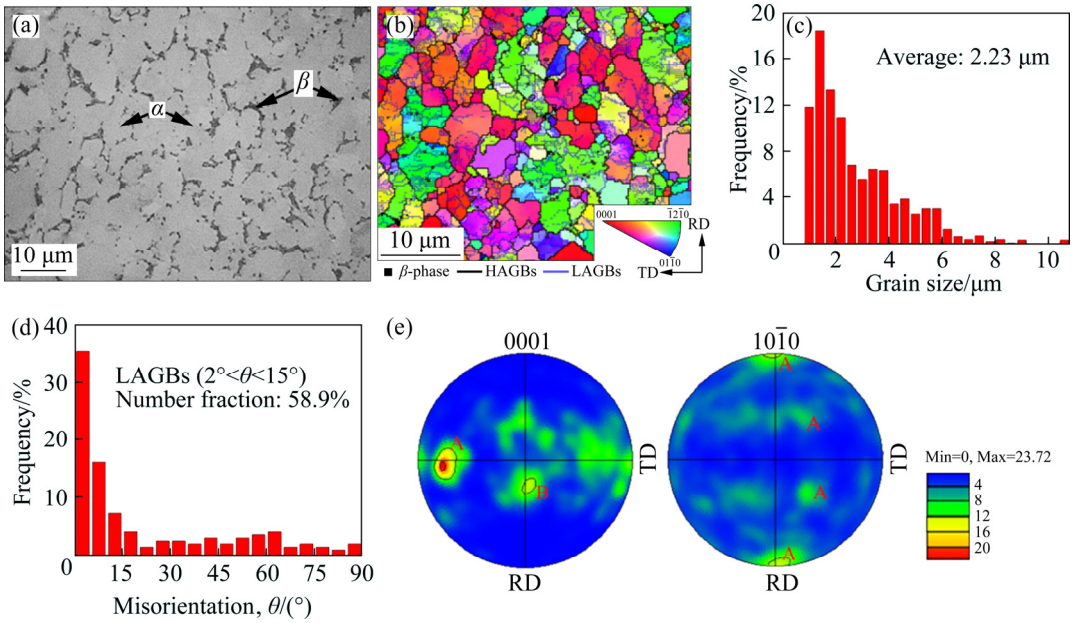

Fig. 2 Characterization of initial TA32 sheet: (a) Optical microstructure; (b) IPF; (c) Grain size distribution; (d) Misorientation distribution; (e) PFs

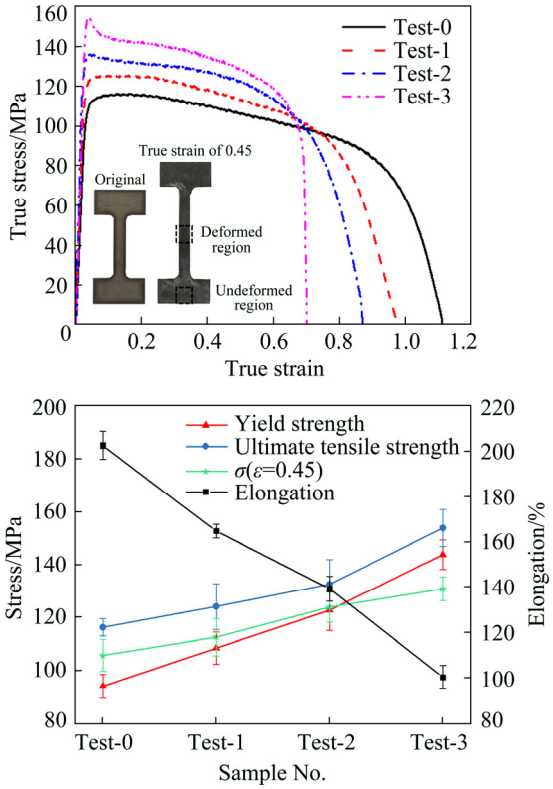

Fig. 3 Hot tensile behavior of different TA32 specimens stretched at 800 °C with strain rate of 0.001 s^{-1}: (a) True stress−strain curves; (b) Tensile properties

of 0.001 s^{-1}. Obviously, the flow curves are significantly affected by the initial microstructure of the material. Figure 3(b) shows tensile properties of different tested specimens with error bars, i.e. yield strength (YS), ultimate tensile strength (UTS), flow stress $\sigma(\varepsilon=0.45)$ and elongation (EL). It can be found that the original sheet exhibits the optimal forming properties with the ultimate tensile strength of 116.3 MPa and elongation of 202.6%. As the heat treatment temperature increases from 800 to 900 °C, the YS increases gradually from 108.5 to 143.8 MPa, and the UTS raises gradually from 124.1 to 153.9 MPa. However, the EL decreases continuously from 164.9% to 100.5%. In order to better understand the reason for different evolutions of tensile properties, the undeformed and deformed regions of tensile specimens with the true strain of 0.45 were used to analyze microstructure evolution and textural change during hot tensile deformation.

3.2 Microstructure evolution during hot tensile deformation

3.2.1 Microstructure of undeformed regions

Figure 4 shows the optical microstructures and the corresponding IPFs of undeformed regions of tensile specimens with the true strain of 0.45. The microstructures of the grip section were approximately considered as the initial microstructures before tensile deformation. It is clearly noticed that the microstructure of each specimen is mainly composed of equiaxed α phase and intergranular β phase. For Test-0 specimen, a number of fine equiaxial α grains appear at grain boundaries as marked with a black circle shown in Fig. 4(a_2). It may be extrapolated as the occurrence of static recrystallization (SRX) through the evolution of subgrain structures with LAGBs into grains with HAGBs. The high energy stored in the initial structure provides a driving force for the occurrence of SRX [23]. For Test-1, Test-2 and Test-3 specimens, the α grain size increases continuously with the increase of heat treatment temperature, and the number of LAGBs in coarse grains is reduced significantly. This suggests that increasing temperature promotes the subgrain coalescence and the formation of the HAGBs. The growth of α grains leads to the increase of material strength during hot deformation, which can be attributed to the fact that the effect of grain boundary sliding exceeds dislocation slip in the process of high temperature deformation [24,25]. The increase of grain size results in the decrease of grain boundary per unit area, which reduces the ability of grain boundary sliding. On the other hand, dynamic recrystallization (DRX) plays a softening role in the deformation process, and the DRX kinetics decreases with the increase of initial grain size [26]. Similar results have been obtained in the studies of QIN et al [27] and SARKAR et al [28].

The details of volume fraction and average grain size of α and β phases in undeformed regions of the tested specimens are shown in Fig. 5(a). The average α grain sizes in undeformed regions of Test-0, Test-1, Test-2 and Test-3 specimens are 2.08, 2.61, 3.69 and 6.06 μm, respectively. The phase volume fraction of each specimen changes slightly because the heat treatment temperature is much lower than the phase transition point. The misorientation distribution and LAGBs number fraction in undeformed regions of tested specimens were calculated, as shown in Fig. 5(b). With the increase of heat treatment temperature, the intergranular misorientation changed gradually

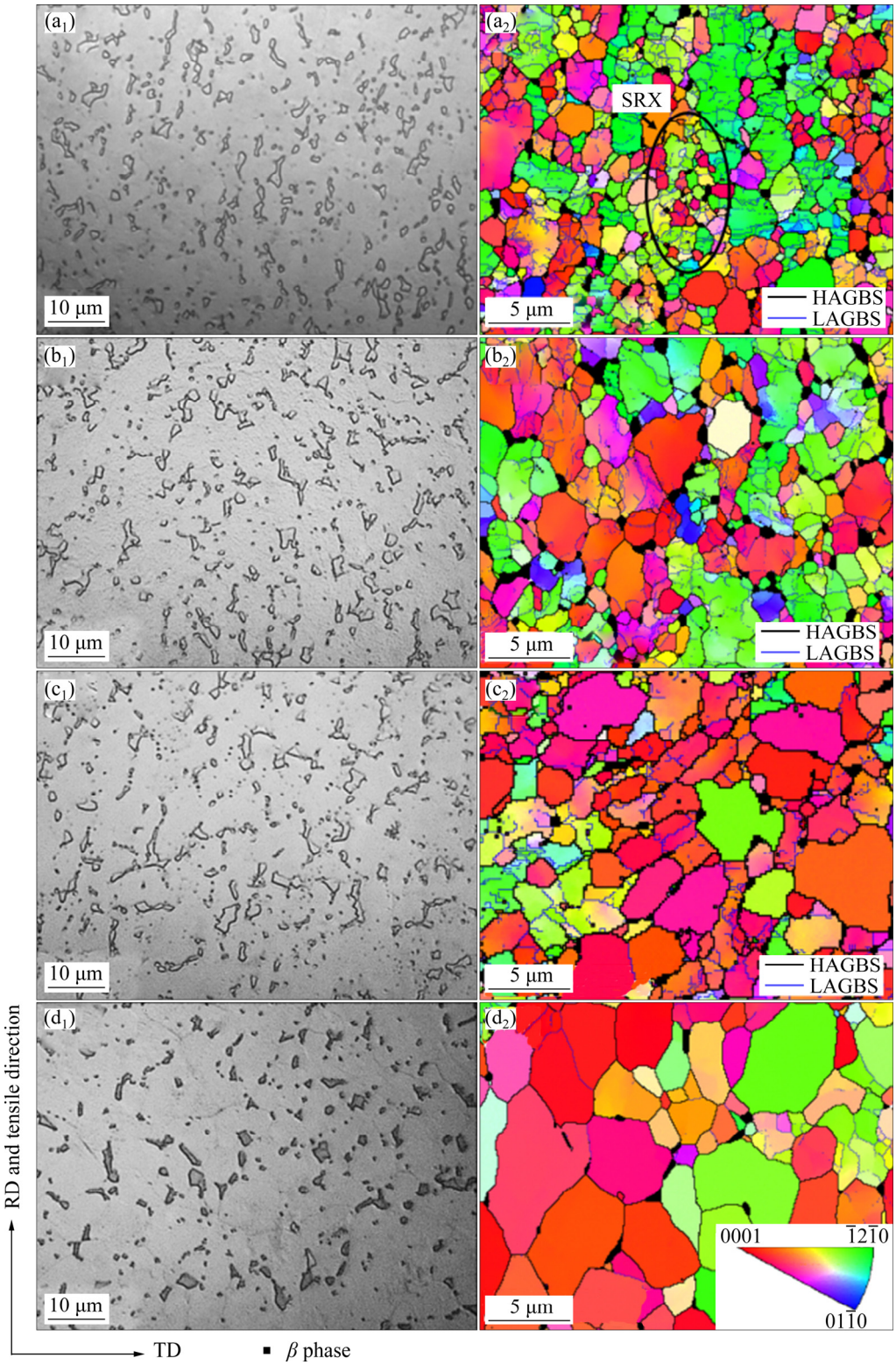

Fig. 4 Optical microstructures (a_1−d_1) and corresponding IPFs (a_2−d_2) of undeformed regions of tensile specimens with true strain of 0.45: (a_1, a_2) Test-0; (b_1, b_2) Test-1; (c_1, c_2) Test-2; (d_1, d_2) Test-3

from LAGBs to HAGBs. The decrease of LAGBs frequency is closely related to the dislocation density. The evolution of dislocation density can be reflected by the geometrically necessary dislocation (GND) density, and the details of the calculation process of GND density have been described by elsewhere [29,30]. Figure 6 shows the GND density maps of undeformed regions of tensile specimens.

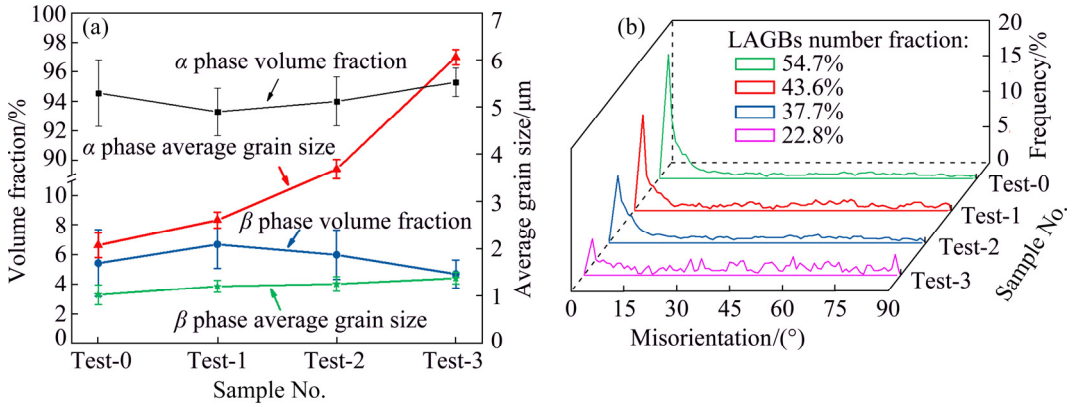

Fig. 5 Microstructure characterization of undeformed regions of different TA32 alloy specimens: (a) Volume fraction and average grain size of α and β phases; (b) Misorientation distribution

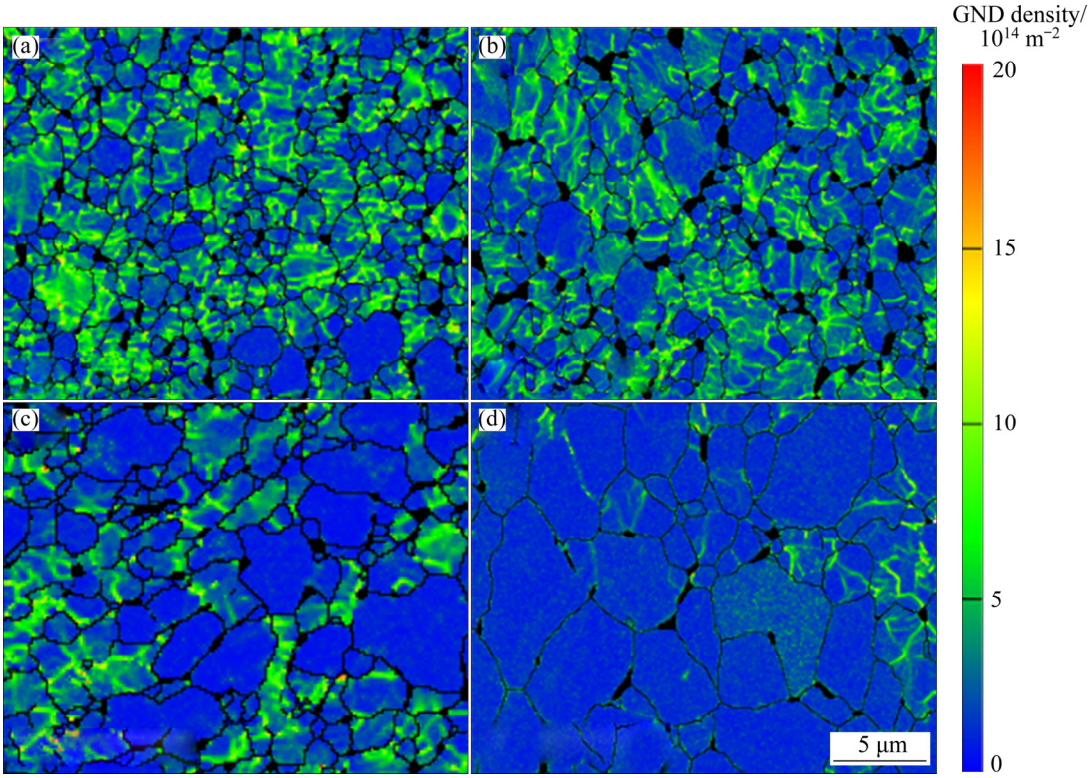

Fig. 6 GND density maps of undeformed regions of tensile specimens with true strain of 0.45: (a) Test-0; (b) Test-1; (c) Test-2; (d) Test-3

It can be clearly seen that the significant decrease in GND density, indicating the aggregation and growth of subgrains during SRX, accelerates the annihilation of dislocations in grains, consequently resulting in a lower fraction of LAGBs.

The orientation of IPFs is with respect to normal direction (ND), and different colors represent different crystal orientations. It can be seen that the color of fine recrystallized grains in Fig. 4(a_1) prefers red, which indicates that the $\langle 0001 \rangle$ orientation of recrystallized grains is parallel to ND. And a lot of substructures and LAGBs exist in the green grains, which indicates that the $\langle \bar{1}2\bar{1}0 \rangle$ orientation of deformed grains is parallel to ND. With increasing heat treatment temperature, the deformed grains in the initial structures are gradually replaced by coarse recrystallized grains without substructures.

3.2.2 Microstructure of deformed regions

Figure 7 shows the optical microstructures and the corresponding IPFs of the deformed regions of

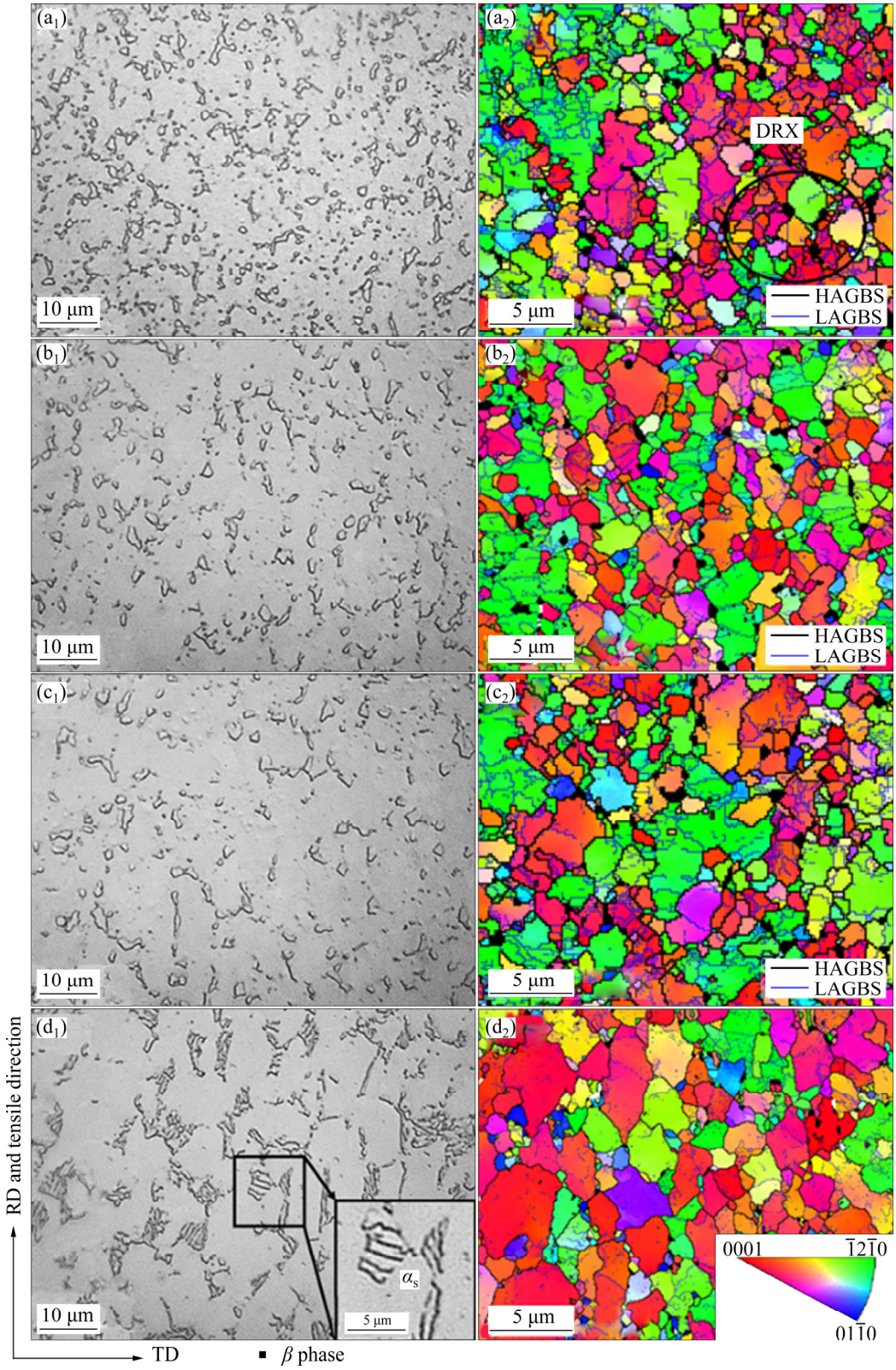

Fig. 7 Optical microstructures (a_1−d_1) and corresponding IPFs (a_2−d_2) of deformed regions of tensile specimens with true strain of 0.45: (a_1, a_2) Test-0; (b_1, b_2) Test-1; (c_1, c_2) Test-2; (d_1, d_2) Test-3

tensile specimens with the true strain of 0.45. After the hot deformation, the initial coarse grains are obviously elongated along the tensile direction, which indicates that the hot deformation mechanism of TA32 alloy is dominated by grain boundary sliding. And a lot of LAGBs are

generated at the interior of deformed grains, which suggests that the dislocation motion also plays a significant role in hot deformation and can be considered as a coordinated process for grain boundary sliding. For Test-0 specimen, the number of fine equiaxial grains at coarse grain boundaries and triple junctions increases drastically, as marked with black circle shown in Fig. 7(a_2), which is a typical feature of dynamic recrystallization [31]. The DRX process refines the α grains in tested specimens and increases the fraction of HAGBs. The increase of HAGBs is very favorable to grain boundary sliding between grains, which makes the material present relatively low flow stress and sound plasticity. However, due to the annihilation and rearrangement of a large number of dislocations as well as the coarsening of α grains during heat treatment, the deformation ability provided by grain boundary sliding and dislocation motion in Test-1, Test-2 and Test-3 specimens gradually decreases with the increase of heat treatment temperature, which results in the increase of flow stress. For Test-3 specimen, many lamellar secondary α grains appear during the hot tensile process, which is magnified in the bottom right corner of Fig. 7(d_1). The formation of lamellar structure is due to the $\beta \rightarrow \alpha'$ martensite transformation happening during quenching in water after TA32 alloy is heat-treated at 900 °C, and subsequent hot deformation results in the decomposition of martensite into α and β phases according to the Burgers orientation relationship and many crystal defects are generated, which promotes the nucleation of secondary α phase at the defect and accompanied by the precipitation of small β phase [32−34]. During deformation, the lamellar α grains can effectively block the mobile dislocations, which accordingly improves the strength [35].

The details of volume fraction and average grain size of α and β phases in deformed regions of the tested specimens are shown in Fig. 8(a). The average α grain sizes in deformed regions of Test-0, Test-1, Test-2 and Test-3 specimens are 1.81, 2.43, 2.88 and 3.78 μm, respectively. Compared with the undeformed regions, the grain size is significantly reduced due to the effect of DRX. The phase volume fraction of each specimen has little change with the same deformation condition. The misorientation distribution and LAGBs number fraction in deformed regions of tested specimens were calculated, as shown in Fig. 8(b). The fraction of LAGBs for Test-0 specimen dropped from 54.7% to 50.6% due to the occurrence of DRX. However, for Test-1, Test-2 and Test-3 specimens, due to the reduction of dislocation density in heat treatment, a large number of dislocations are generated in deformed grains during hot deformation to coordinate the plastic deformation, which results in the increase of LAGBs. The GND density maps of the deformed regions of tensile specimens also corroborate the increase of dislocation density after tensile tests, as shown in Fig. 9.

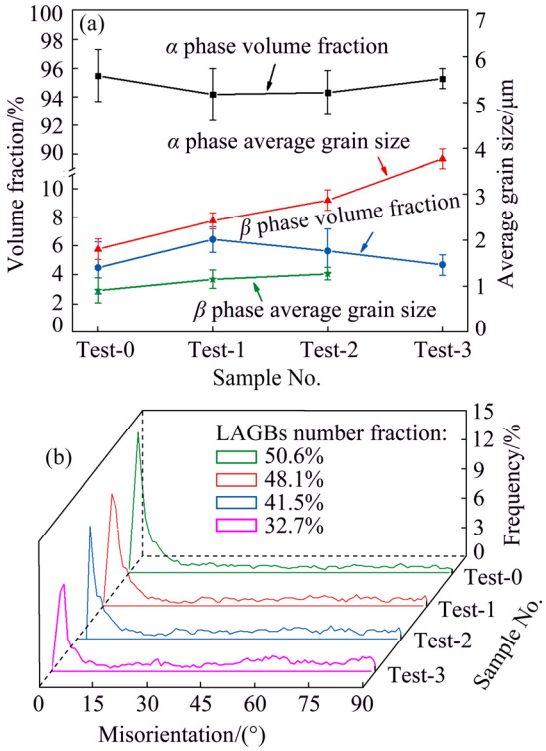

Fig. 8 Microstructure characterization of deformed regions of different TA32 alloy specimens: (a) Volume fraction and average grain size of α and β phases; (b) Misorientation distribution

In addition, it can be observed from IPFs that the fraction of green grains in the deformed regions is more than that in the undeformed regions, which indicates that grain rotation occurred during tensile deformation, and the $\langle \bar{1}2\bar{1}0 \rangle$ orientation of most grains tends to be parallel to ND due to the activation of favorable slip system.

3.3 Quantitative relationship between microstructure and properties

Generally, high temperature creep deformation in crystal materials may occur by processes

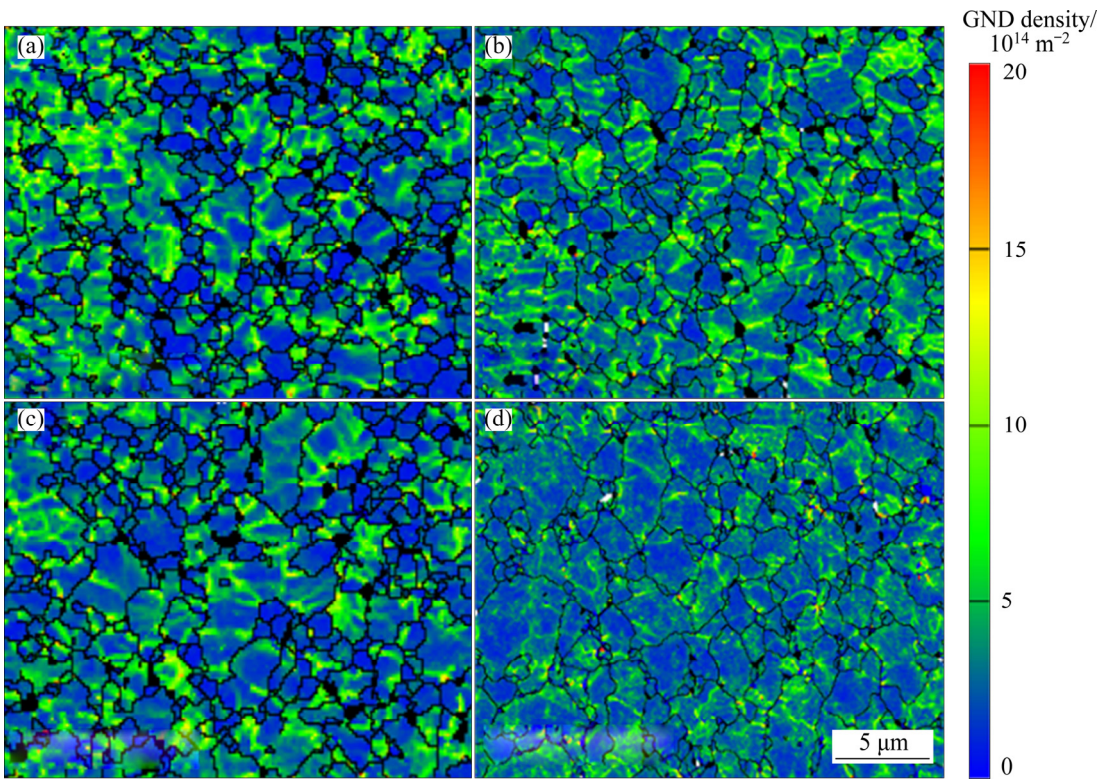

Fig. 9 GND density maps of deformed regions of tensile specimens with true strain of 0.45: (a) Test-0; (b) Test-1; (c) Test-2; (d) Test-3

associated with intragranular dislocation motion, grain boundary sliding, and diffusion creep. The tensile properties are usually characterized in the form of the following equation [36]:

$$\dot{\varepsilon} = \frac{ADGb}{kT}\left(\frac{\sigma}{G}\right)^{n_1}\left(\frac{b}{d}\right)^{\mu} \tag{1}$$

where $\dot{\varepsilon}$ is the steady-state strain rate, A is a constant, D is the appropriate diffusion coefficient, G is the shear modulus, b is the Burgers vector component, k the is Boltzman constant, T is the thermodynamic temperature, σ is the applied stress, d is the grain size, n_1=1/m is a constant termed the stress exponent (m is the strain rate sensitivity exponent which is about 0.25 in this work [4]), and μ is the grain size exponent. In this study, according to the microstructure evolution of TA32 alloy sheet during the hot tensile deformation, it is assumed that the grain size exponent of the β phase is equal to that of the α phase due to the low volume fraction and small grain size of β phase.

At high temperature, for multiphase or two-phase materials, the coordinated deformation of grains of each phase should be considered. The effect of the volume fraction of phases on material properties can be predicted with two simple assumptions and utilization of the law of mixtures rule. The first one is that the strain is the same in both phases (iso-strain), known as the Voigt Estimate, and the second one is that stress is the same in both phases (iso-stress), known as the Reuss Estimate [37,38]. In this work, following the method of BAI et al [39], the total strain rate can be written as

$$\dot{\varepsilon}_{\mathrm{p}} = f_{\alpha}\dot{\varepsilon}_{\mathrm{p},\alpha} + f_{\beta}\dot{\varepsilon}_{\mathrm{p},\beta} \tag{2}$$

where $\dot{\varepsilon}_{\mathrm{p}}$ is the total plastic strain rate, $\dot{\varepsilon}_{\mathrm{p},\alpha}$ is the plastic strain rate of α phase, $\dot{\varepsilon}_{\mathrm{p},\beta}$ is the plastic strain rate of β phase, f_{α} and f_{β} are the volume fractions of α and β phases, respectively. By simplifying the coefficient in Eq. (1), the average grain size d is translated into dimensionless quantity by replacing it with the relative grain size $\bar{d}(\bar{d} = d/d_0)$, in which d_0 is the average grain size of Test-0 specimen, and the plastic strain rates of α and β phases can be obtained as follows:

$$\begin{cases} \dot{\varepsilon}_{\mathrm{p},\alpha} = \left(\dfrac{\sigma}{K_{\alpha}}\right)^{n_1}(\bar{d}_{\alpha})^{-\mu} \\ \dot{\varepsilon}_{\mathrm{p},\beta} = \left(\dfrac{\sigma}{K_{\beta}}\right)^{n_1}(\bar{d}_{\beta})^{-\mu} \end{cases} \tag{3}$$

where K_α and K_β are the strength constants of α and β phases, respectively. Equations (2) and (3) can be integrated into one equation which is described as

$$\dot{\varepsilon}_{\mathrm{p}} = f_\alpha \left(\frac{\sigma}{K_\alpha}\right)^{n_1} (\bar{d}_\alpha)^{-\mu} + f_\beta \left(\frac{\sigma}{K_\beta}\right)^{n_1} (\bar{d}_\beta)^{-\mu} \tag{4}$$

According to Fig. 5(a), since the volume fraction and the average grain size of β phase change slightly, the latter term in Eq. (4) can be approximated as a constant Z. For the Test-0 specimen, Eq. (4) can be written as

$$\dot{\varepsilon}_{\mathrm{p}} = f_{\alpha,0} \left(\frac{\sigma_0}{K_\alpha}\right)^{n_1} + Z_0 \tag{5}$$

where $f_{\alpha,0}$ is the volume fraction of α phase in Test-0 specimen, σ_0 is the initial yield stress during hot tensile deformation, and Z_0 is a constant. Equation (4) is divided by Eq. (5), and taking natural logarithms on both sides of the equation, the following equation can be obtained:

$$\ln\left[\frac{f_\alpha}{f_{\alpha,0}}\left(\frac{\sigma}{\sigma_0}\right)^{n_1}\right] = \mu \ln \bar{d}_\alpha + \ln\left(\frac{\dot{\varepsilon}_{\mathrm{p}} - Z}{\dot{\varepsilon}_{\mathrm{p}} - Z_0}\right) \tag{6}$$

By introducing the volume fraction and average grain size of α phase and the corresponding yield strength from Fig. 8(a) and Fig. 3(b) to Eq. (6), respectively, the slope of linear fitting curve of $\ln\left[\frac{f_\alpha}{f_{\alpha,0}}\left(\frac{\sigma}{\sigma_0}\right)^{n_1}\right]$ versus $\ln \bar{d}_\alpha$ (see Fig. 10) for the grain size exponent μ is 1.57. Besides, due to the fact that the main element in α and β phases is titanium, the material properties for both phases are considered to be similar, and it has been assumed that K_α=1.11K_β [39]. Therefore, the value of K_α was calculated to be 549.58 MPa.

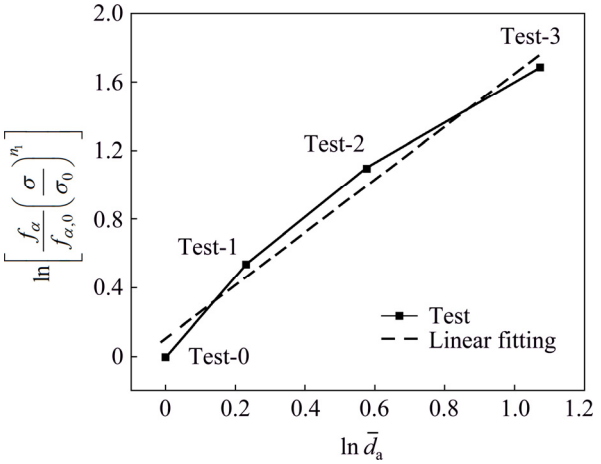

Fig. 10 Relationship between $\ln\left[\frac{f_\alpha}{f_{\alpha,0}}\left(\frac{\sigma}{\sigma_0}\right)^{n_1}\right]$ and $\ln \bar{d}_\alpha$ for different TA32 specimens

In order to verify the accuracy of the solution results, the flow stresses of Test-0, Test-1 and Test-2 tensile specimens at the true strain of 0.45 were predicted by employing the data in Fig. 3(b) (Test-3 specimen was neglected due to the precipitation of secondary lamellar α phase during hot tensile deformation). Using correlation coefficient (R), average absolute relative error ($AARE$) and root mean square error ($RMSE$) can be calculated by Eq. (7) to evaluate the predicted results.

$$\begin{cases} R = \dfrac{\sum_{i=1}^{N}(\sigma_i^{\mathrm{e}} - \bar{\sigma}^{\mathrm{e}})(\sigma_i^{\mathrm{p}} - \bar{\sigma}^{\mathrm{p}})}{\sqrt{\sum_{i=1}^{N}(\sigma_i^{\mathrm{e}} - \bar{\sigma}^{\mathrm{e}})^2 \sum_{i=1}^{N}((\sigma_i^{\mathrm{p}} - \bar{\sigma}^{\mathrm{p}})^2}} \\ AARE = \dfrac{1}{N}\sum_{i=1}^{N}\dfrac{|\sigma_i^{\mathrm{e}} - \sigma_i^{\mathrm{p}}|}{\sigma_i^{\mathrm{e}}} \times 100\% \\ RMSE = \sqrt{\dfrac{1}{N}\sum_{i=1}^{N}(\sigma_i^{\mathrm{e}} - \sigma_i^{\mathrm{p}})^2} \end{cases} \tag{7}$$

where N is the number of the data points used for the comparison, σ_i^{e} denotes the experimental stress and σ_i^{p} denotes the predicted stress using the proposed Eq. (4), $\bar{\sigma}^{\mathrm{e}}$ and $\bar{\sigma}^{\mathrm{p}}$ are the mean values of the experimental and predicted stresses, respectively. The comparison between predicted and experimental results of the flow stress and the fitting error is shown in Fig. 11. It can be seen that the predicted stress is slightly lower than the experimental stress, and the error increases gradually with the increase of heat treatment temperature. The value of R is 0.9918, which means a goodness of the predicted results, and the $AARE$ and $RMSE$ reflect that the error of the predicted results is within an acceptable range, which are 4.64% and 5.58 MPa, respectively.

It can be seen from the pole figures in Fig. 2(e) that there are two strong texture components in the initial sheet, and as we all known that texture plays an essential role in plastic deformation of titanium alloy, which is closely related to the deformation mechanism [40,41]. Therefore, the

error of predicted results can be attributed to the influence of texture on the deformation behavior, and the effect of texture evolution on tensile properties during hot tensile deformation is discussed below.

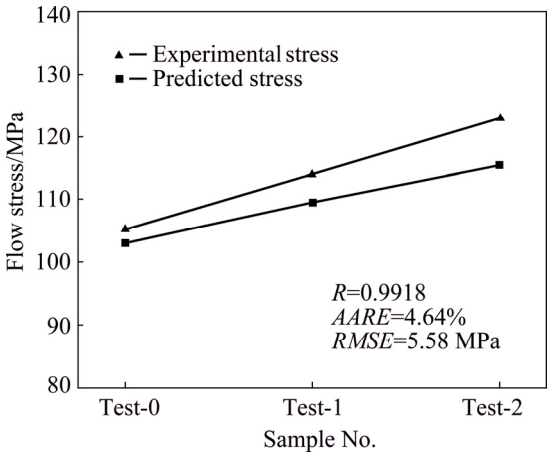

Fig. 11 Comparison between predicted and experimental flow stresses with true strain of 0.45 for test specimens during hot tensile deformation

3.4 Texture evolution during hot tensile deformation

According to the above analysis, the texture of TA32 specimens is affected by recrystallization, grain growth and $\alpha\rightarrow\beta\rightarrow\alpha$ transformation, which result in the orientation of some crystals to deviate from the original position and gather in a specific direction. To better discuss textural evolution during hot tensile deformation, orientation distribution function (ODF) was used to analyze changes in orientation distribution of TA32 titanium alloy sheet.

Figure 12 depicts the ODF sections at φ_2=0° of the undeformed regions of tensile specimens with the true strain of 0.45. It can be seen that the main peak is centered at the texture component A $(\bar{1}2\bar{1}2)[10\bar{1}0]$, and the secondary peak appears in the texture component B $(\bar{1}2\bar{1}5)[1\bar{2}13]$. With the increase of heat treatment temperature, the intensity of component A decreases while that of component B increases, which may be attributed to the growth of recrystallized grains. According to Fig. 4, we can

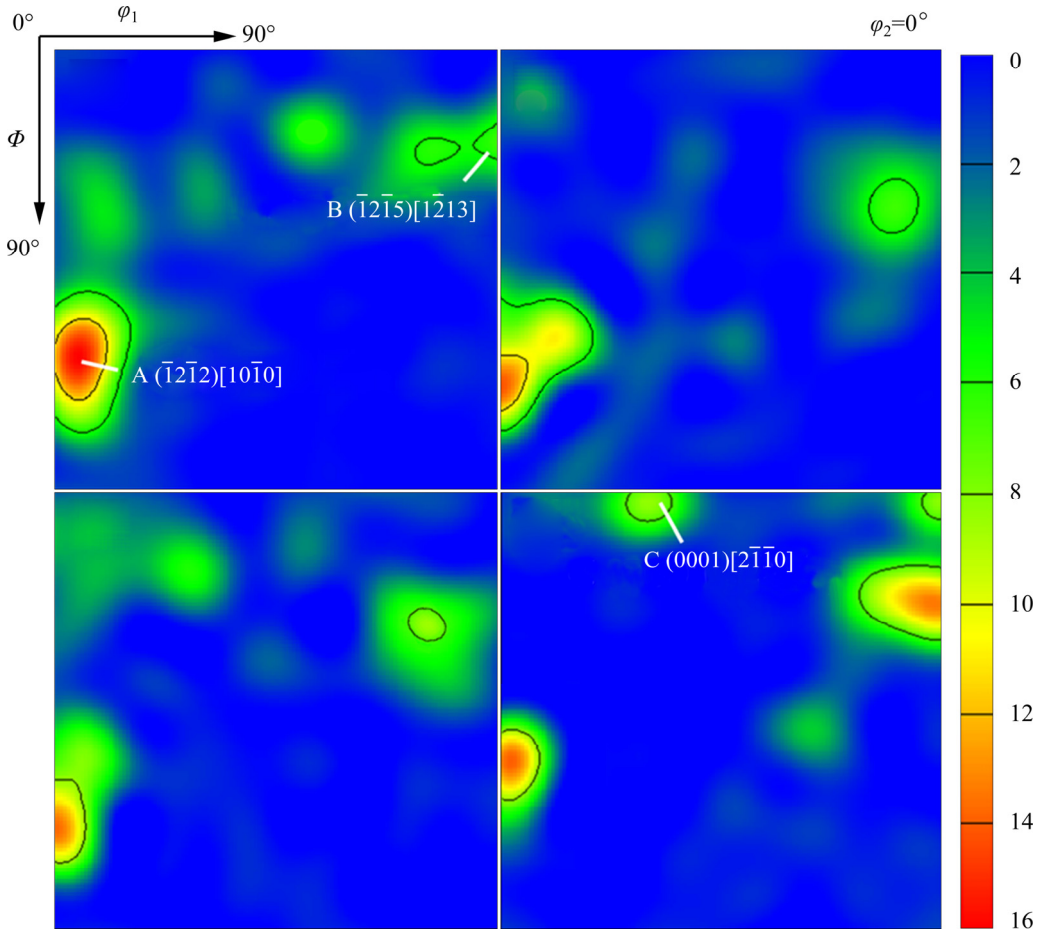

Fig. 12 ODF sections at φ_2=0° of undeformed regions of tensile specimens with true strain of 0.45: (a) Test-0; (b) Test-1; (c) Test-2; (d) Test-3

extrapolate that textures A and B are deformation texture and recrystallization texture, respectively. The growth of recrystallized grains leads to the fact that the content of deformed grains gradually decreases, which results in the weakening of texture A and the strengthening of texture B. In addition, for Test-3 specimen, α grains are significantly coarsened as the heat treatment temperature reaches 900 °C, and some grains prefer to growing along the basal orientation [42−44]. Therefore, a small amount of basal texture component C $(0001)[2\bar{1}\bar{1}0]$ appears in Fig. 12(d).

Figure 13 depicts the ODF sections at φ_2=0° of the deformed regions of tensile specimens with the true strain of 0.45. Distinct changes in texture appear after the tensile deformation. It can be found that texture component A of the undeformed region is almost completely transformed to a transverse texture component D $(11\bar{2}0)[1\bar{1}00]$, which is a typical deformation texture generated in titanium alloy during hot deformation [40]. The intensity of texture B is also decreased compared with the corresponding undeformed region. And the texture intensity of deformed regions is relatively scattered due to the dynamic recrystallization process. In Fig. 13(d), the formation of lamellar secondary α phase follows the Burgers orientation relationship $(0001)//(110)_\beta$ and $[11\bar{2}0]//[111]_\beta$ [45], which results in the augmentation of component C in Test-3 specimen during deformation. The weakening and change of the textures in Fig. 13 indicate that the orientation of some initial grains has rotated to coordinate with grain boundary sliding during hot deformation.

Generally, the ease of slip on a particular system is quantified by the critical resolved shear stress (CRSS), and the slip system can be activated when the resolved shear stress (RSS, τ) is larger than this critical value [46]. According to many studies on the CRSS in titanium alloy [47,48], basal $\langle a\rangle$ and prismatic $\langle a\rangle$ slip systems have the lowest CRSS, and the pyramidal $\langle c+a\rangle$ slip system has the

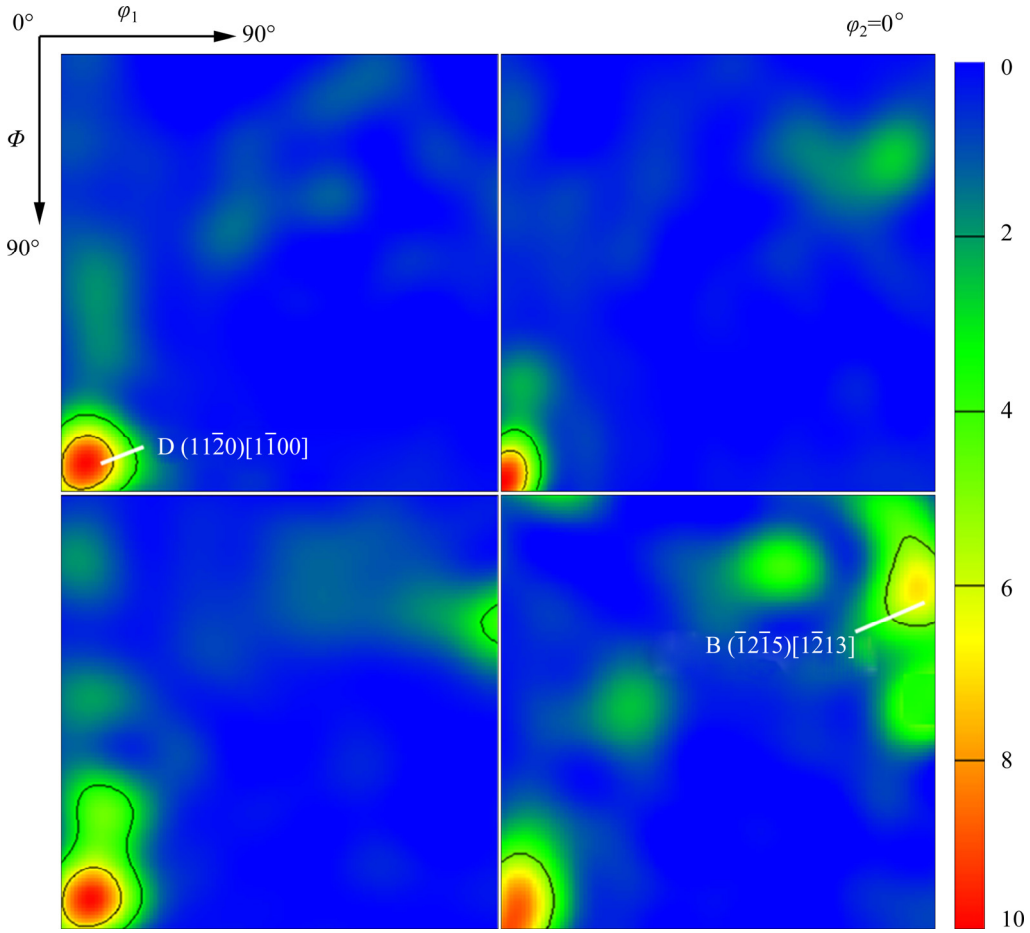

Fig. 13 ODF sections at φ_2=0° of deformed regions of tensile specimens with true strain of 0.45: (a) Test-0; (b) Test-1; (c) Test-2; (d) Test-3

highest value of CRSS. The RSS is calculated by $\tau=M\sigma$, where M is the Schmid factor and σ is the applied flow stress.

In Fig. 14, Schmid factor maps of basal $\langle 11\bar{2}0\rangle\{0001\}$, prismatic $\langle a\rangle\langle 11\bar{2}0\rangle\{10\bar{1}0\}$ and pyramidal $\langle c+a\rangle\langle 11\bar{2}3\rangle\{10\bar{1}1\}$ slip systems are generated for tested specimens. The Schmid factor values of tensile specimens for different slip systems are shown in Table 2. It can be found that $\vec{a}$ -type and $\vec{c}+\vec{a}$ -type slip systems have been activated. The low Schmid factor of basal slip system is due to the fact that the c-axis of most grains is perpendicular to the tensile direction, which restrains the activation of basal slip system. The high Schmid factors of prismatic $\langle a\rangle$ and pyramidal $\langle c+a\rangle$ slip systems indicate that the orientation of α crystals in tested specimens is favorable to the activation of these two slip systems. However, since the CRSS of prismatic $\langle a\rangle$ slip system is much lower than that of pyramidal $\langle c+a\rangle$ slip system, it can be concluded that the prismatic slip system plays a dominant role in the process of hot deformation.

The schematic diagram of texture evolution of TA32 titanium alloy sheet during hot tensile deformation is shown in Fig. 15. For Test-0 specimen, a large amount of near prismatic oriented texture A in the original sheet promotes the initiation of the prismatic slip system, which results in the low flow stress and high elongation. For heat-treated specimens, with the increase of heat treatment temperature, the intensity of near basal oriented texture B gradually increases due to the growth of recrystallized grains. Compared with

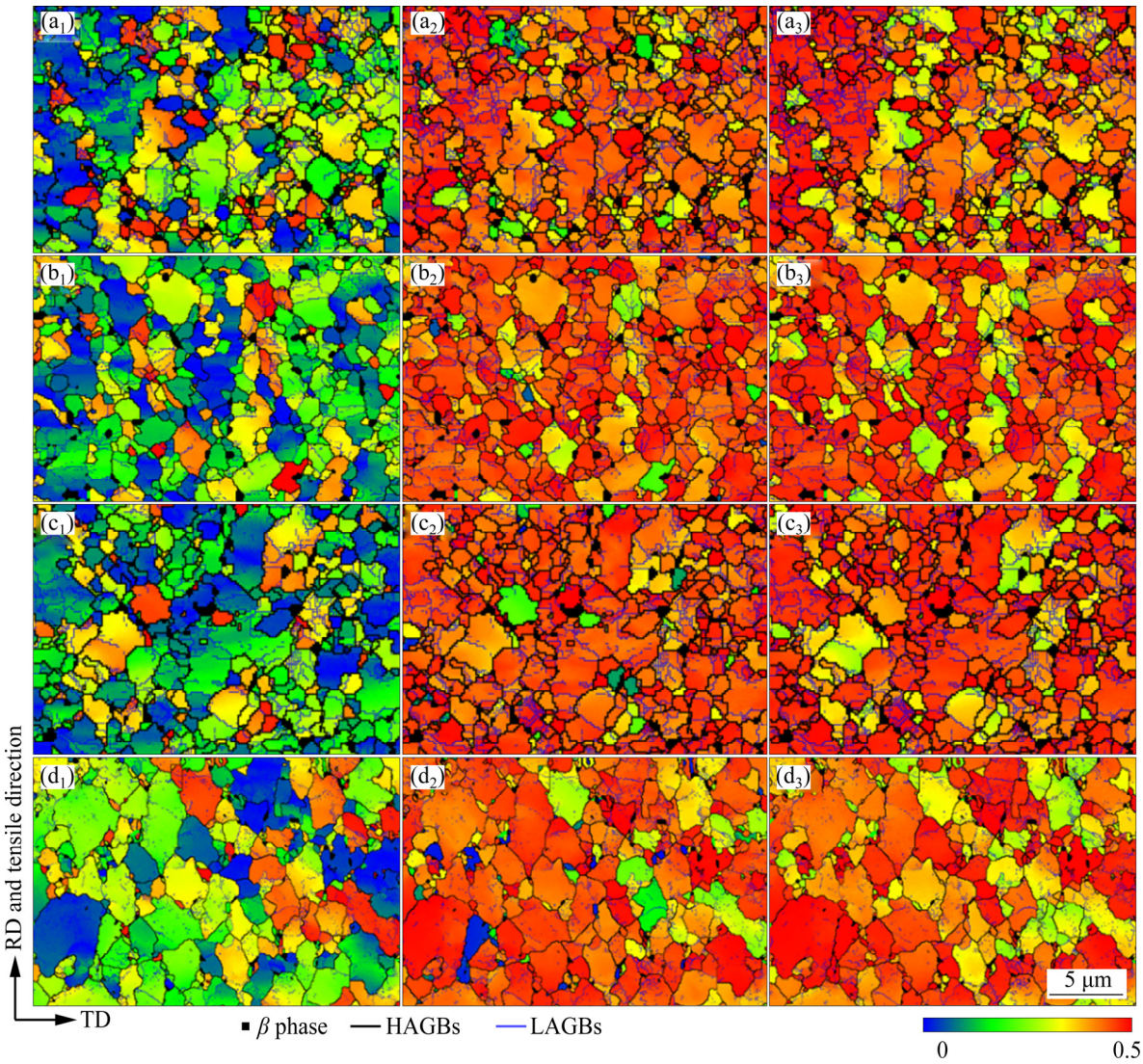

Fig. 14 Schmid factor maps of basal $\langle a\rangle$, prismatic $\langle a\rangle$ and pyramidal $\langle c+a\rangle$ slip systems in deformed regions of tested specimens: (a_1−a_3) Test-0; (b_1−b_3) Test-1; (c_1−c_3) Test-2; (d_1−d_3) Test-3

Table 2 Schmid factors of tensile specimens for different slip systems

Sample No.	Schmid factor		
	Basal ⟨*a*⟩	Prismatic ⟨*a*⟩	Pyramidal ⟨*c*+*a*⟩
Test-0	0.187	0.437	0.406
Test-1	0.198	0.424	0.386
Test-4	0.239	0.403	0.376
Test-5	0.262	0.385	0.362

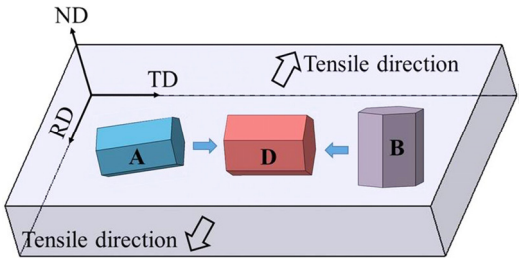

Fig. 15 Schematic diagram of texture evolution during hot tensile deformation

texture A, the crystal orientation of texture B is unfavorable to the activation of prismatic slip system, which leads to an increase in the flow stress.

4 Conclusions

(1) The deformation behaviors of various heat-treated TA32 alloys are different. The original sheet exhibits the optimal forming properties with the ultimate tensile strength of 116.3 MPa and elongation of 202.6%. With the heat treatment temperature raising from 800 to 900 °C, the ultimate tensile strength increases from 124.1 to 153.9 MPa, while the elongation decreases from 164.9% to 101.5%.

(2) During the hot tensile deformation, the deformation mechanism of TA32 alloy is dominated by the sliding of high angle grain boundaries, and dislocation motion also plays a significant role in hot deformation and can be considered as an accommodation process for grain boundary sliding. The coarsening of grains and the annihilation of dislocations in heat-treated specimens weaken the deformation ability of material, which leads to the increase in flow stress.

(3) The flow stress is obviously affected by the volume fraction and grain size of α and β phases. Based on the creep equation, the grain size exponent and α phase strength constant of TA32 alloy are calculated to be 1.57 and 549.58 MPa, respectively. The flow stress during hot tensile deformation can be accurately predicted by combining with the corresponding phase volume fraction and grain size.

(4) The hot deformation behavior of TA32 alloy is also dependent on the orientation of predominant α phase, and the main deformation mode is the activation of prismatic ⟨*a*⟩ slip system. The orientation of texture $(\bar{1}2\bar{1}2)[10\bar{1}0]$ in the specimen is more favorable to the activation of prismatic slip system than that of texture $(\bar{1}2\bar{1}5)[1\bar{2}13]$. Therefore, the decrease of near prismatic oriented texture in heat-treated specimens results in the enhancement of strength.

References

[1] BANERJEE D, WILLIAMS J. Perspective on titanium science and technology [J]. Acta Materialia, 2013, 61: 844−879.

[2] WANG Ke-huan, LIU Gang, ZHAO Jie, WANG Jian-long, YUAN Shi-jian. Formability and microstructure evolution for hot gas forming of laser-welded TA15 titanium alloy tubes [J]. Materials and Design, 2016, 91: 269−277.

[3] ZHAO Zi-bo, WANG Qing-jiang, LIU Jian-rong, YANG Rui. Effect of heat treatment on the crystallographic orientation evolution in a near-α titanium alloy Ti60 [J]. Acta Materialia, 2017, 131: 305−314.

[4] FAN Rong-lei, CHEN Ming-he, WU Yong, XIE Lan-sheng. Prediction and experiment of fracture behavior in hot press forming of a TA32 titanium alloy rolled sheet [J]. Metals, 2018, 8: 985−999.

[5] WU Yong, LIU Gang, WANG Kai, LIU Zhi-qiang, YUAN Shi-jian. The deformation and microstructure of Ti−3Al−2.5V tubular component for non-uniform temperature hot gas forming [J]. The International Journal of Advanced Manufacturing Technology, 2017, 88: 2143−2152.

[6] WANG Tao, GUO Hong-zhen, WANG Yan-wei, PENG Xiao-na, ZHAO Yan, YAO Ze-kun. The effect of micro-structure on tensile properties, deformation mechanisms and fracture models of TG6 high temperature titanium alloy [J]. Materials Science and Engineering A, 2011, 528: 2370−2379.

[7] SINGH A K, SCHWARZER R A. Evolution of texture during thermomechanical processing of titanium and its alloys [J]. Transactions of the Indian Institute of Metals, 2008, 61: 371−387.

[8] LI Ping, DING Yong-gen, YAO Peng-peng, XUE Ke-min, LI Cheng-ming. Study on high-temperature flow behavior and substructure and texture evolution of TA15 titanium alloy [J]. Journal of Materials Engineering and Performance, 2016, 25: 3439−3447.

[9] ZENG Zhi-peng, ZHANG Yan-shu, JONSSON S.

Microstructure and texture evolution of commercial pure titanium deformed at elevated temperatures [J]. Materials Science and Engineering A, 2009, 513: 83−90.

[10] LIU Zhang-guang, LI Pei-jie, GENG Lin-lin, LIU Tai-ying, GAO Hai-tao. Microstructure and texture evolution of TA32 titanium alloy during superplastic deformation [J]. Materials Science and Engineering A, 2017, 699: 71−80.

[11] JIA Wei-ju, ZENG Wei-dong, ZHOU Yi-gang, LIU Jian-rong, WANG Qing-jiang. High-temperature deformation behavior of Ti60 titanium alloy [J]. Materials Science and Engineering A, 2011, 528: 4068−4074.

[12] GAO Peng-fei, MEI Zhan, FAN Xiao-guang, LEI Zhen-ni, CAI Yang. Hot deformation behavior and microstructure evolution of TA15 titanium alloy with nonuniform microstructure [J]. Materials Science and Engineering A, 2017, 689: 243−251.

[13] WANJARA P, JAHAZI M, MONAJATI H, YUE S, IMMARIGEON J P. Hot working behavior of near-α alloy IMI834 [J]. Materials Science and Engineering A, 2005, 396: 50−60.

[14] WANG Zhe, WANG Xin-nan, ZHU Zhi-shou. Characterization of high-temperature deformation behavior and processing map of TB17 titanium alloy [J]. Journal of Alloys and Compounds, 2017, 692: 149−154.

[15] LIN J. Selection of material models for predicting necking in superplastic forming [J]. International Journal of Plasticity, 2003, 19: 469−481.

[16] YANG Lei, WANG Bao-yu, LIU Gang, ZHAO Hui-jun, XIAO Wen-chao. Behavior and modeling of flow softening and ductile damage evolution in hot forming of TA15 alloy sheets [J]. Materials and Design, 2015, 85: 135−148.

[17] ALABORT E, PUTMAN D, REED R C. Superplasticity in Ti−6Al−4V: Characterisation, modelling and applications [J]. Acta Materialia, 2015, 95: 428−442.

[18] BACHE M R, EVANS W J. Impact of texture on mechanical properties in an advanced titanium alloy [J]. Materials Science and Engineering A, 2001, 319: 409−414.

[19] AHMADIAN P, ABBASI S M, MORAKABATI M. The role of initial α-phase orientation on tensile and strain hardening behavior of Ti−6Al−4V alloy [J]. Materials Today Communications, 2017, 13: 332−345.

[20] CHEN Can, CHEN Ming-he, XIE Lan-sheng, GONG Zong-hui, YE Jian-hua. Numerical and experimental investigations of the hot stamping process for complex aircraft skin parts composed of TA32 high-temperature titanium alloy using an Arrhenius-type constitutive model [J]. The International Journal of Advanced Manufacturing Technology, 2019 103: 807−817.

[21] WANG Qing-jiang, LIU Jian-rong, YANG Rui. High temperature titanium alloys: Status and perspective [J]. Journal of Aeronautical Materials, 2014, 34: 1−26.

[22] LEYENS C, PETERS M, LEYENS C, PETERS M. Titanium and titanium alloys: Fundamentals and applications [M]. Weinheim: Wiley-VCH, 2003.

[23] WANG Ke, WU Ming-yu, YAN Zhi-bing, LI Dong-rong, XIN Ren-long, LIU Qing. Microstructure evolution and static recrystallization during hot rolling and annealing of an equiaxed-structure TC21 titanium alloy [J]. Journal of Alloys and Compounds, 2018, 752: 14−22.

[24] VANDERHASTEN M, RABET L, VERLINDEN B. Deformation mechanism of Ti6Al4V during tensile behaviour at low strain rate [J]. Journal of Materials Engineering and Performance, 2007, 16: 208−212.

[25] ROY S, SUWAS S. Deformation mechanisms during superplastic testing of Ti−6Al−4V−0.1B alloy [J]. Materials Science and Engineering A, 2013, 574: 205−217.

[26] OHADI D, PARSA M H, MIRZADEH H. Development of dynamic recrystallization maps based on the initial grain size [J]. Materials Science and Engineering A, 2013, 565: 90−95.

[27] QIN Qing-feng, TAN Ying-xin, YANG Yong-biao, WANG Qiang, REN Gang. Influence of grain size on hot deformation behaviour of 7A04 aluminium alloy [J]. Hot Working Technology, 2016, 45: 59−63.

[28] SARKAR A, PRASAD M J N V, MURTY S V S N. Effect of initial grain size on hot deformation behaviour of Cu−Cr−Zr−Ti alloy [J]. Materials Characterization, 2020, 160: 110−112.

[29] KUMAR S S S, PAVITHRA B, SINGH V, GHOSAL P, RAGHU T. Tensile anisotropy associated microstructural and microstructural evolution in a metastable beta titanium alloy [J]. Materials Science and Engineering A, 2019, 747: 1−16.

[30] MOUSSA C, BERNACKI M, BESNARD R, BOZZOLO N. Statistical analysis of dislocations and dislocation boundaries from EBSD data [J]. Ultramicroscopy, 2017, 179: 63−72.

[31] HE Dong, ZHU Jing-chuan, LAI Zhong-hong, LIU Yong, YANG Xia-wei. An experimental study of deformation mechanism and microstructure evolution during hot deformation of Ti−6Al−2Zr−1Mo−1V alloy [J]. Materials and Design, 2013, 46: 38−48.

[32] ZHU Shuai, YANG He, GUO Liang-gang, FAN Xiao-guang. Effect of cooling rate on microstructure evolution during α/β heat treatment of TA15 titanium alloy [J]. Materials Characterization, 2012, 70: 101−110.

[33] SUN Feng, LI Jin-shan, KOU Hong-chao, TANG Bin, CAI Jian-ming. Effect of α' martensite on microstructure refinement after $\alpha+\beta$ isothermal treatment in a near-α titanium alloy Ti60 [J]. Journal of Materials Engineering and Performance, 2015, 24: 1945−1952.

[34] SADEGHPOUR S, ABBASI S M, MORAKABATI M, BRUSCHI S. Correlation between alpha phase morphology and tensile properties of a new beta titanium alloy [J]. Materials and Design, 2017, 121: 24−35.

[35] LI Cong, CHEN Jian, LI Wei, REN Yan-jie, HE Jian-jun, SONG Z X. Effect of heat treatment variations on the microstructure evolution and mechanical properties in a β metastable Ti alloy [J]. Journal of Alloys and Compounds, 2016, 684: 466−473.

[36] MUKHERJEE A K. An examination of the constitutive equation for elevated temperature plasticity [J]. Materials Science and Engineering A, 2002, 322: 1−22.

[37] KIM W J, CHUNG S W, CHUNG C S, KUM D. Superplasticity in thin magnesium alloy sheets and deformation mechanism maps for magnesium alloys at elevated temperatures [J]. Acta Materialia, 2001, 49: 3337−3345.

[38] NEMAT-NASSER S. Plasticity: A treatise on the finite deformation of heterogeneous inelastic materials [M]. Cambridge: Cambridge University Press, 2004.

[39] BAI Qian, LIN Jian-guo, DEAN T A, BALINT D S, GAO Tao, ZHANG Zhu. Modelling of dominant softening mechanisms for Ti−6Al−4V in steady state hot forming conditions [J]. Materials Science and Engineering A, 2013, 559: 352−358.
[40] LIN Peng, FENG Ai-han, YUAN Shi-jian, LI Ge-ping, SHEN Jun. Microstructure and texture evolution of a near-α titanium alloy during hot deformation [J]. Materials Science and Engineering A, 2013, 563: 16−20.
[41] AHMADIAN P, ABBASI S M, MORAKABATI M. Effect of initial texture and grain size on geometrically necessary dislocations density distribution during uniaxial compression of Ti6Al4V [J]. Materials Today Communications, 2018, 14: 263−272.
[42] HUMPHREYS F J, HATHERLY M. Recrystallization and related annealing phenomena [M]. 2nd ed. Amsterdam: Elsevier, 2004.
[43] SINGH A K, SCHWARZER R A. Evolution of texture during thermomechanical processing of titanium and its alloys [J]. Transactions of the Indian Institute of Metals, 2008, 61: 371−387.
[44] BHATTACHARYYA J J, AGNEW S R, MURALIDHARAN G. Texture enhancement during grain growth of magnesium alloy AZ31B [J]. Acta Materialia, 2015, 86: 80−94.
[45] HE Dong, ZHU Jing-chuan, ZAEFFERER S, RAABE D, LIU Yong, LAI Zhong-hong, YANG Xia-wei. Influences of deformation strain, strain rate and cooling rate on the Burgers orientation relationship and variants morphology during $\beta\rightarrow\alpha$ phase transformation in a near-α titanium alloy [J]. Materials Science and Engineering A, 2012, 549: 20−29.
[46] LI H, MASON D E, BIELER T R, BOEHLERT C J, CRIMP M A. Methodology for estimating the critical resolved shear stress ratios of α-phase Ti using EBSD-based trace analysis [J]. Acta Materialia, 2013, 61: 7555−7567.
[47] FAN X G, JIANG X Q, ZENG X, SHI Y G, GAO P F, ZHAN M. Modeling the anisotropy of hot plastic deformation of two-phase titanium alloys with a colony microstructure [J]. International Journal of Plasticity, 2018, 104: 173−195.
[48] WON J W, PARK C H, HONG S G, LEE C S. Deformation anisotropy and associated mechanisms in rolling textured high purity titanium [J]. Journal of Alloys and Compounds, 2015, 651: 245−254.

TA32 钛合金板材在热拉伸变形过程中显微组织、力学性能与织构的关系

范荣磊，武 永，陈明和，谢兰生

南京航空航天大学 直升机传动技术重点实验室，南京 210016

摘 要：研究 TA32 钛合金板材在 800 °C 热拉伸变形过程中显微组织、力学性能和织构之间的关系。在实验中，原始板材表现出较低的流动应力和良好的塑性，随着热处理温度的升高，材料的抗拉强度增加，伸长率降低。TA32 钛合金的变形机制是以大角晶界滑移为主，并通过位错运动协调变形。热处理试样中晶粒粗化和位错湮灭削弱材料的变形能力，从而导致流动应力的增加。基于高温蠕变方程，建立显微组织与流变应力的定量关系。TA32 合金的晶粒影响因子和 α 相强度系数分别为 1.57 和 549.58 MPa。通过综合相应的相体积分数和晶粒尺寸可以准确预测材料的流动应力。此外，TA32 合金的变形行为还与 α 相晶粒的取向相关，其主要滑移方式为柱面<a>滑移系的开动。热处理试样中近柱面织构的减少同样导致材料强度的提高。

关键词：TA32 钛合金板材；热拉伸变形；显微组织演变；力学性能；织构

(Edited by Wei-ping CHEN)